 CMES, vol.96, no.6, pp.379-407, 2013

Simulations of Three-dimensional Thermal Residual Stress and Warpage in Injection Molding

Xuejuan Li[1,2], **Jie Ouyang**[2,3], **Wen Zhou**[2]

Abstract: The three-dimensional (3D) mathematical models for thermal residual stress and warpage are proposed in injection molding, in which the temperature model is rebuilt by considering the phase-change effect to improve the computational accuracy. The 3D thermal residual stress model is transformed into the incremental displacement model so that the boundary conditions can be imposed easily. A modified finite element neural network (FENN) method is used for solving 3D warpage model based on the advantages of finite element method and neural network. The influence of phase-change on temperature is discussed. The numerical simulations of thermal residual stress and warpage are realized, and the influences of processing parameters on thermal residual stress and warpage are studied. The numerical results are in accordance with the results in related literature and the theoretic analysis.

Keywords: 3D, phase-change, thermal residual stress, warpage, processing parameter.

1 Introduction

Thermal residual stress and warpage affect seriously mechanical properties and visual quality of products [Shen and Li (2003)]. However, it is very difficult to control these defects effectively before polymer being processed since polymer melts experience complex changes in injection molding process. With the rapid development of computer technology, numerical simulation has become a powerful method in improving quality and process technology of plastic products. However, so far the numerical simulations of thermal residual stress and warpage mainly adopt the Generalized Hele-Shaw (GHS) flow model based on mid-plane mesh model during

[1] School of Science, Xi'an University of Architecture and Technology, Xi'an, 710055, PR China.
[2] School of Science, Northwestern Polytechnical University, Xi'an, 710129, PR China, jieouyang@nwpu.edu.cn
[3] Corresponding author. Email: jieouyang@nwpu.edu.cn

the injection and packing stage. GHS model cannot obtain the complete information of physical quantities. Moreover, it leads to compute thermal residual stress only under the hypotheses of thin-wall cavity, and compute warpage only by the way of decoupling two-dimensional plane deformation and one-dimensional normal bending. Therefore, it is necessary to develop three-dimensional (3D) mathematical models and computational methods.

So far the numerical simulations of the thermal residual stress mainly adopt elastic model, viscoelastic model and creep model based on GHS flow model in packing and cooling stage. Boitou, Agassant and Vincent adopted elastic model to calculate thermal residual stress considering thermal shrinkage and the frozen-in pressure [Boitou, Agassant and Vincent (1995)]. Then Jansen, Titomanlio and Pantani proposed a simple elastic model for residual stresses and shrinkage of a thin solidifying product and studied the shrinkage based on different processing parameters [Jansen and Titomanlio (1996); Jansen, Pantani and Titomanlio (1998)]. However, since the elastic model ignores viscosity, a viscoelastic model can give more accurate results than an elastic model. Therefore, some researchers realized the importance of relaxation effect and proposed some viscoelastic model for thermal residual stress. Baaijens, Chang and Chiou adopted linear Maxwell model [Baaijens (1991)] and Kaye-Bernstein-Kearsley-Zapas(K-BKZ) model [Chang and Chiou (1995)] to calculate thermal residual stress, respectively. Moreover, Bushko and Vijay proposed a linear thermo-viscoelastic model based on the assumption that the polymer was a thermo-rheologically simple thermo-viscoelastic material [Bushko and Vijay (1995)]. Thereafter, this model was used in many references. Zoetelief, Douven and Ingen Housz investigated the influence of packing stage on the thermal residual stress [Zoetelief, Douven and Ingen Housz (1996)]. The finite difference method and finite element method were adopted to compute thermal residual stress in the literatures [Chen, Lama and Li (2000), Kamal, Lai-Fook and Hernandez-Aguilar (2002)], respectively. Some researchers study the influences of processing parameters [Wang and Young (2005)], polymer type [Young (2004)], gate location [Lee, Huang, Yang and Kim (2006)] etc. on thermal residual stress. Zhou, Xi and Liu calculated thermal residual stress based on surface flow model [Zhou, Xi and Liu (2008)]. In literature [Frederico, Patrick, Gerrit, António and Han (2010)], the linear thermo-viscoelastic model was applied to gas-assisted injection molding. Wu, Zhao and Shen emphasized the importance of relaxation effect and proposed the creep model [Wu, Zhao and Shen (2008)]. By comparison, the elastic model ignores the viscosity and the calculation results are a little bigger. The linear thermo-viscoelastic model is widely applied in the calculation of thermal residual stress, but the creep model is rarely used.

Moreover, phase-change of the polymer melt is very important in injection molding

[Yang, Fu, Yang, Huang, Yang and Feng (2008); Yang, Fu, Yang, Liang, Hu and Yang (2009)], but it is always ignored in calculation of thermal residual stress. The mathematical models, which are currently used for phase-change phenomena can fall into three categories [Truex (2011)]: sharp interface models, phase field models, and enthalpy models. The sharp interface models [Kosec and Sarler (2009)] require sharp front tracking and are typically used in one-dimensional problems. The phase field models require a priori knowledge of the free energy density function and can not be widely used. By comparison, the enthalpy models overcome the above limitations and have several flexible forms.

For the numerical simulation of warpage, many researchers decoupled the warpage into two-dimensional plane deformation and one-dimensional normal bending. Then they adopted different elements in finite element method (FEM) to calculate the decoupled problem based on flat shell element model. For example, the constant strain triangular element and the discrete Kirchhoff triangular element were used to calculate the warpage [Guo, Ruan, Peng and Li (2002); Li and Zhou (2004)]. Liu, Zhou and Li gave the modified flat shell element model for applying to the surface model, and then adopted plane membrane element and bending plate element for plane deformation and normal bending, respectively [Liu, Zhou and Li (2009)]. Moreover, Zhou, Wang, Li, and Li built the warpage model based on surface mesh model directly [Zhou, Wang, Li, and Li (2011)].

Therefore, we calculate 3D thermal residual stress based on the linear thermo-viscoelastic model and set up the temperature model of phase-change in this paper. Moreover, we transform the 3D model into the incremental displacement model so that the boundary conditions can be imposed easily, and adopt the enthalpy transformation model and finite volume method (FVM) to calculate temperature based on the phase-change Finally, we construct the 3D warpage model based on the residual stress model [Choi and Im (1999)] after demolding to calculate warpage for 3D injection molding. Then we modify the finite element neural network [Yagawa and Okuda (1996); Ramuhalli, Udpa and Udpa (2005)] (FENN) for solving 3D warpage model.

2 Governing equations

The flow of polymer melts is governed by the conservation of mass, momentum and energy equations, together with a viscosity model and a state equation. The governing equations can be non-dimensionalized via $\mathbf{x}^* = \mathbf{x}/L$, $\mathbf{u}^* = \mathbf{u}/U$, $t^* = tU/L$, $\rho^* = \rho/\rho_r$, $p^* = p/(\rho_r U^2)$, $T^* = T/T_r$, $\eta^* = \eta/\eta_r$, $C_p^* = C_p/C_0$, $\kappa^* = \kappa/\kappa_0$. Where L, U, ρ_r, T_r and η_r are length scale, velocity scale, density scale, temperature scale and viscosity scale, respectively. As a matter of convenience, the

mark "*" is omitted and, and the governing equations (1), (2) and (3) can be written as,

$$\rho_t + \nabla \cdot (\rho \mathbf{u}) = 0 \tag{1}$$

$$\rho \mathbf{u}_t + \rho \mathbf{u} \cdot \nabla \mathbf{u} = \eta / Re \nabla^2 \mathbf{u} - \nabla \cdot p + \eta / (3Re) \nabla (\nabla \cdot \mathbf{u}) \tag{2}$$

$$Pe (\rho T_t + \rho \mathbf{u} \cdot \nabla T) = \nabla^2 T + Br \eta \dot{\gamma}^2 \tag{3}$$

where the subscript t denotes time derivative, ρ is the density, $\mathbf{u}$ is the velocity vector, p is the pressure, η is the viscosity, $\dot{\gamma}$ is the shearing rate, C_p is the specific heat,κ is thermal conductivity and T is the temperature. Reynolds number $Re = \rho_r UL / \eta_r$, Peclet number $Pe = \rho_r C_p UL / \kappa$, Brinkman number $Br = \eta_r U^2 / (\kappa T_r)$.

The polymer viscosity model is

$$\eta (T, \dot{\gamma}, p) = \frac{\eta_0 (T, p)}{1 + \left(\eta_0 \dot{\gamma} / \tau^*\right)^{1-n}} \tag{4}$$

where $\eta_0 (T, p)$ is the melt viscosity under zero-shear-rate conditions, τ^* is the model constant that shows the shear stress rate, from which the pseudoplastic behavior of the melt starts. n is the model constant. A WLF expression is considered to determine the zero-shear-viscosity of the melt

$$\eta_0 = D_1 \exp \left(\frac{-A_1 \left(T - \hat{T}\right)}{A_2 + \left(T - \hat{T}\right)} \right) \tag{5}$$

where $\hat{T} = D_2 + D_3 \cdot P$; $A_2 = \tilde{A}_2 + D_3 \cdot P$.

A state equation is introduced to satisfy the completeness of governing equations. Tait state equation can be represented as follows

$$\frac{1}{\rho} = V (p, T) = V_0 (T) \left\{ 1 - C \ln \left[1 + \frac{p}{B(T)} \right] \right\} + V_t (T, p) \tag{6}$$

The related terms can be expressed as follows:

$$V_0(T) = \begin{cases} b_{1m} + b_{2m}(T - b_5) & \text{if } T > T_t \\ b_{1s} + b_{2s}(T - b_5) & \text{if } T < T_t \end{cases} \tag{7}$$

$$B(T) = \begin{cases} b_{3m} \exp[-b_{4m}(T - b_5)] & \text{if } T > T_t \\ b_{3s} \exp[-b_{4s}(T - b_5)] & \text{if } T < T_t \end{cases} \tag{8}$$

$$V_t(T, p) = \begin{cases} 0 & \text{if } T > T_t \\ b_7 \exp[b_8(T - b_5) - b_9 p] & \text{if } T < T_t \end{cases} \tag{9}$$

where $C = 0.0894$ is universal constant; b_1, b_2, b_3, b_4, b_5, b_6, b_7, b_8, b_9 are material constants and the subscript m and s identify the melt and solid; $T_t = b_5 + b_6 p$ is the glass transition temperature of the melt.

The simulation of the flow process is used to calculate the pressure of the liquid phase and the frozen-in stresses. The weakly-compressible Crank-Nicolson-based split (WCNBS) scheme for finite element method (FEM) formulation is presented in our previous work [Li, Ouyang, Li and Ren (2012)] and is used to simulate the flow process of injection modeling. On the other hand, calculations of the energy equation determine the temperature histories in the entire domain including both the liquid and solid phases. The temperature histories are the key factor in calculating thermal residual stress in injection modeling. To obtain a more reasonable temperature field, we calculate the temperature based on phase-change.

3 Temperature Calculation Based on Phase-change

3.1 Enthalpy Transformation Model

Under constant pressure, the enthalpy H is defined by $C_p(T) = \partial H / \partial T$. In enthalpy transformation model, the relation between T and H is [Yang, Fu, Yang, Huang, Yang and Feng (2008); Yang, Fu, Yang, Liang, Hu and Yang (2009)]

$$T(H) = \begin{cases} lT_s + \dfrac{H}{C_{p,s}}, & H \le 0 \\ T_s + \dfrac{H \cdot \Delta T}{L_h + C_{p,f} \cdot \Delta T}, & 0 < H < L_h + C_{p,f}\Delta T \\ T_s + \dfrac{H}{C_{p,l}} - \dfrac{L_h + (C_{p,f} - C_{p,l})\Delta T}{C_{p,l}}, & H \ge L_h + C_{p,f}\Delta T \end{cases} \tag{10}$$

where L_h is the latent heat. The subscript s, l, f denote solid phase, liquid phase and the mushy region, respectively. By introducing Kirchhoff temperature $T_{kir} = \Gamma(H)H + S(H)$, the enthalpy transformation model of energy equation can be written as

$$Pe\left(\frac{\partial \rho H}{\partial t} + \frac{\partial \rho u H}{\partial x} + \frac{\partial \rho v H}{\partial y} + \frac{\partial \rho w H}{\partial z}\right) = \frac{\partial^2 \Gamma(H) H}{\partial x^2} + \frac{\partial^2 \Gamma(H) H}{\partial y^2} + \frac{\partial^2 \Gamma(H) H}{\partial z^2} + \frac{\partial^2 S(H)}{\partial x^2} + \frac{\partial^2 S(H)}{\partial y^2} + \frac{\partial^2 S(H)}{\partial z^2} + Br\eta\dot{\gamma}^2 \tag{11}$$

where

$$\Gamma(H)=\begin{cases}\dfrac{k_s}{C_{p,s}}, & H\le 0\\ \dfrac{k_f\Delta T}{L_h+C_{p,f}\Delta T}, & 0<H<L_h+C_{p,f}\Delta T\\ \dfrac{k_l}{C_{p,l}}, & H\ge L_h+C_{p,f}\Delta T\end{cases},$$

$$S(H)=\begin{cases}0, & H\le 0\\ 0, & 0<H<L_h+C_{p,f}\Delta T\\ -k_l\dfrac{L_h+(C_{p,f}-C_{p,l})\Delta T}{C_{p,l}} & H\ge L_h+C_{p,f}\Delta T\end{cases}.$$

3.2 Enthalpy Transformation Model solvers for FVM formulation

FVM had been proven highly effective in solving the energy equation in our previous works [Li, Ouyang, Li, Wu and Yang (2011); Li Ouyang, Li and Ren (2012)]. So FVM is still used to solve the enthalpy transformation model and the discretization can be written as

$$a_P H_P = a_E H_E + a_W H_W + a_N H_N + a_S H_S + a_T H_T + a_B H_B + S_\varphi \tag{12}$$

where S_φ is the source term in the energy equation, and the coefficients a_E, a_W, a_N, a_S, a_T, a_B and a_P can be expressed as

$$\begin{aligned}&a_E = D_e A(|P_e|)+\max(-F_e,0), \quad a_W = D_w A(|P_w|)+\max(F_w,0),\\ &a_N = D_n A(|P_n|)+\max(-F_n,0), \quad a_S = D_s A(|P_s|)+\max(F_s,0),\\ &a_T = D_t A(|P_t|)+\max(-F_t,0), \quad a_B = D_b A(|P_b|)+\max(F_b,0),\end{aligned}$$

$$a_P = a_E + a_W + a_N + a_S + a_T + a_B + Pe\rho\frac{\Delta x\Delta y\Delta z}{\Delta t} \tag{13}$$

where P_e, P_s, P_w, P_n, P_t, P_b are the Péclet numbers on the cell faces; F_e ,F_s ,F_w ,F_n ,F_t ,F_b are the cell faces flux; D_e, D_s, D_w, D_n, D_t, D_b denote diffuse derivatives on the cell faces. The form $A(|P_\Delta|)$ can be different according to the method by which the convection terms are discretized. The upwind scheme(US) is adopted in this paper for strongly convection-dominated problem, so that $A(|P_\Delta|)=1$. And all the above coefficients are formulated as follows

$$F_e = Pe\,(\rho u)_{fe}\Delta y\Delta z, \quad D_e = \Gamma(H)\frac{\Delta y\Delta z}{x_E-x_P}, \quad P_e = \frac{F_e}{D_e}$$

$$
\begin{aligned}
&F_w = Pe\,(\rho u)_{fw}\Delta y\Delta z, \quad D_w = \Gamma(H)\frac{\Delta y\Delta z}{x_P - x_W}, \quad P_w = \frac{F_w}{D_w}\\
&F_n = Pe\,(\rho v)_{fn}\Delta x\Delta z, \quad D_n = \Gamma(H)\frac{\Delta x\Delta z}{y_N - y_P}, \quad P_n = \frac{F_n}{D_n}\\
&F_s = Pe\,(\rho v)_{fs}\Delta x\Delta z, \quad D_s = \Gamma(H)\frac{\Delta x\Delta z}{y_P - y_S}, \quad P_s = \frac{F_s}{D_s}\\
&F_t = Pe\,(\rho w)_{ft}\Delta x\Delta y, \quad D_t = \Gamma(H)\frac{\Delta x\Delta y}{z_T - z_P}, \quad P_t = \frac{F_t}{D_t}\\
&F_b = Pe\,(\rho w)_{fb}\Delta x\Delta y, \quad D_b = \Gamma(H)\frac{\Delta x\Delta y}{z_P - z_B}, \quad P_b = \frac{F_b}{D_b}
\end{aligned}
\tag{14}
$$

3.3 Influence of the phase-change on the temperature

To study the influence of the phase-change on the temperature, we choose the polymer High-Density Polyethylene (HDPE) Sclair 2714, which is made by Nova Chemicals Inc., as fluid. The thermal parameters are obtained from materials data base of Moldflow software. Fig. 1 shows the changes of specific heat (C_p) and thermal conductivity (κ) with temperature (T). From Fig. 1(a), it can be seen that the curve of specific heat exists a sharp at T=106 because of phase-change and it changes little before and after phase-change. The material parameters of HDPE Sclair 2714 are shown in Table 1, Table 2 and Table 3, respectively.

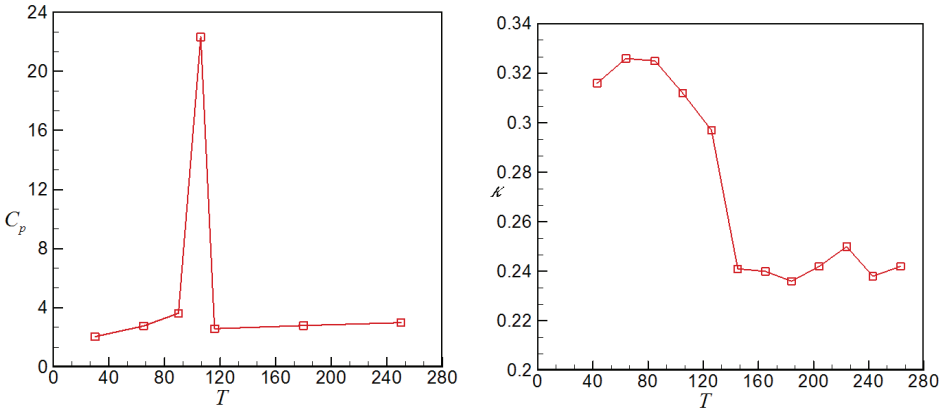

(a) (b)

Figure 1: The changes of specific heat (a) and thermal conductivity (b) with temperature

Table 1: Thermal property parameters

κ_s	κ_l	$C_{p,s}$	$C_{p,l}$	L_h	T_s	T_l
(W/m·°C)	(W/m·°C)	(J/kg·°C)	(J/kg·°C)	(J/kg)	(°C)	(°C)
0.316	0.238	2042.0	2990.0	1.8×10^5	104	108

Table 2: Tait state equation parameters

Parameter	Value	Parameter	Value	Parameter	Value
$b_{1,m}(m^3/\text{kg})$	1.264×10^3	$b_{1,s}(m^3/\text{kg})$	1.12×10^3	$b_7(m^3/\text{kg})$	1.44×10^{-4}
$b_{2,m}(m^3/\text{kg})$	9.847×10^{-7}	$b_{2,s}(m^3/\text{kg·K})$	5.852×10^{-7}	b_8(1/K)	0.1425
$b_{3,m}$(Pa)	1.062×10^8	$b_{3,s}$(Pa)	2.43×10^8	b_9(1/Pa)	2.527×10^{-8}
$b_{4,m}$(1/K)	4.726×10^3	$b_{4,s}$(1/K)	2.339×10^3		
b_5(K)	4.052×10^2	b_6(K/Pa)	1.6×10^{-7}		

Table 3: Cross-WLF viscosity model parameters

Parameter	Value	Parameter	Value
n	0.3794	D_3(K/Pa)	0.1
τ^*(Pa)	105985	A_1	32.344
D_1(Pa·s)	5.769×10^{13}	$\tilde{A}_2$(K)	51.6
D_2(K)	233.15		

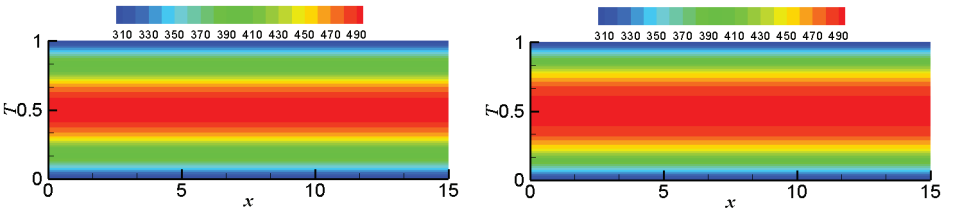

(a) (b)

Figure 2: The temperature contour distributions at t=50: (a) with phase-change, (b) without phase-change

The temperature contour distributions at t=50 are shown in Fig. 2. From Fig. 2, it can be seen that the green color region is wider with phase-change than that without phase-change under the same level contours. Fig. 3 shows the comparisons of temperature with phase-change and without phase-change at different time. We

can clearly see that there is a steep change for the case with phase-change while there is a smooth change for the case without phase-change in phase-change region. The results prove that phase-change has strong influence on temperature.

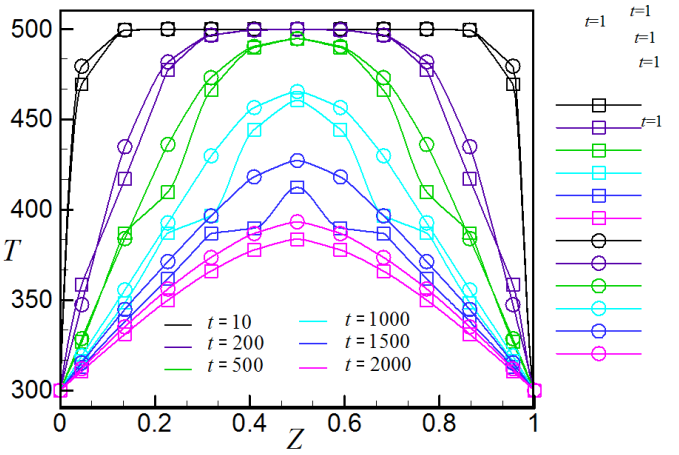

Figure 3: The comparisons of temperature between with phase-change (□) and without phase-change (◯) at different time

4 Thermal Residual Stress Simulations

Polymer melt gradually solidifies with the decrease of temperature during packing and cooling stage of injection molding. Therefore, thermal residual stress is produced when the shrinkage of solid is constrained by mold cavity during solidification, and it is caused by the change of temperature and strain. Moreover, the thermal residual stress is the immediate cause for warpage of products.

4.1 Linear Thermo-viscoelastic Model

To describe the viscoelasticity of polymer in the calculation of thermal stress, a thermo-viscoelastic constitutive model is the reasonable option. It can be written as [Kamal, Lai-Fook and Hernandez-Aguilar (2002)]

$$\boldsymbol{\sigma} = -p^h \mathbf{I} + \boldsymbol{\sigma}^d \tag{15}$$

where, $\boldsymbol{\sigma}$ is the Cauchy stress tensor, p^h is the hydrostatic pressure, $\mathbf{I}$ is the unit-tensor, $\boldsymbol{\sigma}^d$ is the extra stress tensor. p^h can be split into temperature change and

volume shrinkage from temperature change and the expression is

$$p^h = -\frac{1}{3}\mathrm{tr}(\boldsymbol{\sigma}) = \int_0^t \left(\frac{\alpha}{\chi}\dot{T} - \frac{1}{\chi}\mathrm{tr}(\dot{\boldsymbol{\varepsilon}})\right) d\tau \tag{16}$$

where $\boldsymbol{\varepsilon}$ is the strain tensor, α is the bulk thermal expansion coefficient, χ is the isothermal compressibility coefficient. A multi-mode Maxwell model with a linearization of the compressible Leonov model is used to describe the extra stress tensor $\boldsymbol{\sigma}^d$, that is

$$\boldsymbol{\sigma}^d = \sum_{i=1}^{m} 2\int_0^t G_i e^{-(\xi(t)-\xi(\tau))/\theta_i}\dot{\boldsymbol{\varepsilon}}^d d\tau, \quad \xi(\tau) = \int_0^\tau \frac{1}{\alpha_T} ds \tag{17}$$

where G_i and θ_i are the shear modulus and relaxation time of the ith mode of multi-mode Maxwell model; $\xi(\tau)$ and α_T are the modified time scale and the shift factor of the time-temperature superposition principle, respectively.

It has been proved that the elastic modulus of a polymer is influenced by the response time. Time-temperature superposition implies that the response time function of the elastic modulus at a certain temperature resembles the shape of the same functions of adjacent temperatures. The shift factor of polymer is usually expressed as

Williams-Landel-Ferry (WLF) and Arrhenius equations

$$\begin{cases} \lg \alpha_T = \dfrac{-C_1(T-T_0)}{C_2+(T-T_0)}, & T_0 < T < T_0+100 \\ \ln \alpha_T = -C_3(T-T_0), & T < T_0 \end{cases} \tag{18}$$

where C_1, C_2 and C_3 are empirical constant; when T_0 is glass transition temperature or crystallization temperature, C_1 and C_2 usually equal 17.4 and 51.6, respectively.

4.2 Numerical method for thermal residual stress

The pressure and temperature histories should be obtained by the calculations of governing equations before the calculations of thermal residual stresses. However, these quantities are dimensionless. So we transform these dimensionless quantities to dimensional quantities by $p^* = p/(\rho_r U^2)$, $T^* = T/T_r$ in the calculations of thermal residual stresses.

To implement boundary conditions easily during the calculation, the linear thermo-viscoelastic model is transformed into the incremental displacement model. Then the thermal stress is calculated by the relations of displacement-strain and strain-stress. The details of numerical method are given as follows.

We firstly consider the discretization of Eq. (15) in time domain within a typical time sub-interval $[t_n,t_{n+1}]$, and the expressions of $\boldsymbol{\sigma}$ at t_n and t_{n+1} are

$$\boldsymbol{\sigma}_n = -p_n^h\mathbf{I}+\boldsymbol{\sigma}_n^d = -\int_0^{t_n}\left(\frac{\alpha}{\chi}\dot{T}-\frac{1}{\chi}\mathrm{tr}\left(\dot{\boldsymbol{\varepsilon}}\right)\right)d\tau+\sum_{i=1}^{m}2\int_0^{t_n}G_i e^{-(\xi(t)-\xi(\tau))/\theta_i}\dot{\boldsymbol{\varepsilon}}^d d\tau \tag{19}$$

$$\begin{aligned}\boldsymbol{\sigma}_{n+1} &= -p_{n+1}^h\mathbf{I}+\boldsymbol{\sigma}_{n+1}^d \\ &= -\int_0^{t_{n+1}}\left(\frac{\alpha}{\chi}\dot{T}-\frac{1}{\chi}\mathrm{tr}\left(\dot{\boldsymbol{\varepsilon}}\right)\right)d\tau+\sum_{i=1}^{m}2\int_0^{t_{n+1}}G_i e^{-(\xi(t)-\xi(\tau))/\theta_i}\dot{\boldsymbol{\varepsilon}}^d d\tau\end{aligned} \tag{20}$$

Define some increments in $\Delta t_{n+1}=t_{n+1}-t_n$ sub-interva: $\Delta\xi_{n+1}=\xi\left(t_{n+1}\right)-\xi\left(t_n\right)$, $\Delta T_{n+1}=T_{n+1}-T_n$, $\Delta\boldsymbol{\varepsilon}_{n+1}=\boldsymbol{\varepsilon}_{n+1}-\boldsymbol{\varepsilon}_n$, $\Delta\boldsymbol{\varepsilon}_{n+1}^d=\boldsymbol{\varepsilon}_{n+1}^d-\boldsymbol{\varepsilon}_n^d$. The $\boldsymbol{\sigma}_{n+1}$ can be written as

$$\begin{aligned}\boldsymbol{\sigma}_{n+1} &= -\left(\int_0^{t_n}\left(\frac{\alpha}{\chi}\dot{T}-\frac{1}{\chi}\mathrm{tr}\left(\dot{\boldsymbol{\varepsilon}}\right)\right)d\tau+\int_{t_n}^{t_{n+1}}\left(\frac{\alpha}{\chi}\dot{T}-\frac{1}{\chi}\mathrm{tr}\left(\dot{\boldsymbol{\varepsilon}}\right)\right)d\tau\right)\mathbf{I} \\ &\quad+\sum_{i=1}^{m}2\int_0^{t_n}G_i e^{-(\xi(t)-\xi(\tau))/\theta_i}\dot{\boldsymbol{\varepsilon}}^d d\tau+\sum_{i=1}^{m}2\int_{t_n}^{t_{n+1}}G_i e^{-(\xi(t)-\xi(\tau))/\theta_i}\dot{\boldsymbol{\varepsilon}}^d d\tau \\ &= \boldsymbol{\sigma}^*+K^*\mathrm{tr}\left(\Delta\varepsilon_{n+1}\right)\mathbf{I}+2G^*\Delta\boldsymbol{\varepsilon}_{n+1}^d\end{aligned} \tag{21}$$

where

$$\boldsymbol{\sigma}^* = -\left(p_n^h+\beta^*\Delta T_{n+1}\right)\mathbf{I}+\sum_{i=1}^{m}2e^{-\Delta\xi_{n+1}/\theta_i}\int_0^{t_n}G_i e^{-(\xi(t_n)-\xi(\tau))/\theta_i}\dot{\boldsymbol{\varepsilon}}^d d\tau,$$

$$K^* = \frac{1}{\Delta t_{n+1}}\int_{t_n}^{t_{n+1}}\frac{1}{\chi}d\tau,$$

$$\beta^* = \frac{1}{\Delta t_{n+1}}\int_{t_n}^{t_{n+1}}\frac{\alpha}{\chi}d\tau,\quad G^* = \frac{1}{\Delta t_{n+1}}\sum_{i=1}^{m}\int_{t_n}^{t_{n+1}}G_i e^{-(\xi(t_{n+1})-\xi(\tau))/\theta_i}d\tau.$$

The components of the formula (21) are

$$\sigma_{11} = \sigma_{11}^*+K^*\left(\Delta\varepsilon_{11}+\Delta\varepsilon_{22}+\Delta\varepsilon_{33}\right)+2G^*\left(\Delta\varepsilon_{11}-\frac{1}{3}\left(\Delta\varepsilon_{11}+\Delta\varepsilon_{22}+\Delta\varepsilon_{33}\right)\right) \tag{22a}$$

$$\sigma_{22} = \sigma_{22}^*+K^*\left(\Delta\varepsilon_{11}+\Delta\varepsilon_{22}+\Delta\varepsilon_{33}\right)+2G^*\left(\Delta\varepsilon_{22}-\frac{1}{3}\left(\Delta\varepsilon_{11}+\Delta\varepsilon_{22}+\Delta\varepsilon_{33}\right)\right) \tag{22b}$$

$$\sigma_{33} = \sigma_{33}^*+K^*\left(\Delta\varepsilon_{11}+\Delta\varepsilon_{22}+\Delta\varepsilon_{33}\right)+2G^*\left(\Delta\varepsilon_{33}-\frac{1}{3}\left(\Delta\varepsilon_{11}+\Delta\varepsilon_{22}+\Delta\varepsilon_{33}\right)\right) \tag{22c}$$

$$\sigma_{12} = \sigma_{21} = 2G^* \Delta\varepsilon_{12} \tag{22d}$$

$$\sigma_{23} = \sigma_{32} = 2G^* \Delta\varepsilon_{23} \tag{22e}$$

$$\sigma_{13} = \sigma_{31} = 2G^* \Delta\varepsilon_{31} \tag{22f}$$

The relation between stress and strain increments of formulas (22a) $\sim$ (22f) can be written as

$$\boldsymbol{\sigma}_{n+1} = \mathbf{D} \cdot \Delta\boldsymbol{\varepsilon}_{n+1} + \boldsymbol{\sigma}^* \tag{23}$$

where $\boldsymbol{\sigma} = [\sigma_{11}, \sigma_{22}, \sigma_{33}, \sigma_{12}, \sigma_{23}, \sigma_{31}]^T$, $\boldsymbol{\sigma}^* = [\sigma_{11}^*, \sigma_{22}^*, \sigma_{33}^*, \sigma_{12}^*, \sigma_{23}^*, \sigma_{31}^*]^T$,

$\boldsymbol{\varepsilon} = [\varepsilon_{11}, \varepsilon_{22}, \varepsilon_{33}, 2\varepsilon_{12}, 2\varepsilon_{23}, 2\varepsilon_{31}]^T$,

$$\mathbf{D} = \begin{bmatrix} a & b & b & 0 & 0 & 0 \\ b & a & b & 0 & 0 & 0 \\ b & b & a & 0 & 0 & 0 \\ 0 & 0 & 0 & G^* & 0 & 0 \\ 0 & 0 & 0 & 0 & G^* & 0 \\ 0 & 0 & 0 & 0 & 0 & G^* \end{bmatrix}, \text{ where } a = K^* + \tfrac{4}{3}G^*, b = K^* - \tfrac{2}{3}G^*.$$

In linear elastic space, the geometric equation of strain-displacement is

$$\varepsilon_{ij}(x,t) = \frac{1}{2}\left[\frac{\partial u_i(x,t)}{\partial x_j} + \frac{\partial u_j(x,t)}{\partial x_i}\right], \quad i,j = 1,2,3 \tag{24}$$

and the tensor form is

$$\boldsymbol{\varepsilon} = \mathbf{A}\mathbf{d} \tag{25}$$

where

$$\mathbf{d} = [d_1, d_2, d_3]^T, \quad \mathbf{A}^T = \begin{bmatrix} \frac{\partial}{\partial x} & 0 & 0 & \frac{\partial}{\partial y} & 0 & \frac{\partial}{\partial z} \\ 0 & \frac{\partial}{\partial y} & 0 & \frac{\partial}{\partial x} & \frac{\partial}{\partial z} & 0 \\ 0 & 0 & \frac{\partial}{\partial z} & 0 & \frac{\partial}{\partial y} & \frac{\partial}{\partial x} \end{bmatrix}.$$

Due to the linear relationship, the increments of strain and displacement also satisfy the above relation

$$\Delta\boldsymbol{\varepsilon} = \mathbf{A}\Delta\mathbf{d} \tag{26}$$

The equilibrium equation of stress-force is

$$\frac{\partial \sigma_{ij}}{\partial x_j} + F_i = 0, \quad i,j = 1,2,3 \tag{27}$$

and the tensor form is

$$\mathbf{A}^T\boldsymbol{\sigma}+\mathbf{F}=0 \tag{28}$$

where $\mathbf{F}=[F_1,F_2,F_3]^T$ is the body force. Substituting Eq. (23) into Eq. (28) results in the following equation

$$\mathbf{A}^T\left(\mathbf{D}\cdot\Delta\boldsymbol{\varepsilon}_{n+1}+\boldsymbol{\sigma}^*\right)+\mathbf{F}=0 \tag{29}$$

Substituting Eq. (26) into Eq. (29) results in the following equation

$$\left(\mathbf{A}^T\mathbf{D}\mathbf{A}\right)\Delta\mathbf{d}_{n+1}=-\mathbf{A}^T\boldsymbol{\sigma}^*-\mathbf{F} \tag{30}$$

Define $\mathbf{S}=\mathbf{A}^T\mathbf{D}\mathbf{A}$, and the matrix S is

$$\mathbf{S}=\begin{bmatrix} a\frac{\partial^2}{\partial x^2}+G^*\frac{\partial^2}{\partial y^2}+G^*\frac{\partial^2}{\partial z^2} & (b+G^*)\frac{\partial^2}{\partial x\partial y} & (b+G^*)\frac{\partial^2}{\partial x\partial z} \\ (b+G^*)\frac{\partial^2}{\partial x\partial y} & G^*\frac{\partial^2}{\partial x^2}+a\frac{\partial^2}{\partial y^2}+G^*\frac{\partial^2}{\partial z^2} & (b+G^*)\frac{\partial^2}{\partial y\partial z} \\ (b+G^*)\frac{\partial^2}{\partial x\partial z} & (b+G^*)\frac{\partial^2}{\partial y\partial z} & G^*\frac{\partial^2}{\partial x^2}+G^*\frac{\partial^2}{\partial y^2}+a\frac{\partial^2}{\partial z^2} \end{bmatrix}.$$

The **F** equals zero in Eq. (30) in packing and cooling stage of injection molding. The displacements on boundaries are zero until mold cavity pressure reads zero, but since then, free boundary conditions are used in Eq. (30). The displacements are obtained first by solving Eq. (30), followed by the increments of strain by solving Eq. (26), and then thermal residual stress by solving Eq. (23). The 8-nodes hexahedral elements are used in above calculations.

4.3 Results Analysis

The numerical simulation is performed in a Cuboid mold cavity (10×5×1), as shown in Fig. 4. Therefore, we only discuss the calculation of temperature based on phase-change in this paper. The enthalpy transformation model is used to calculate the enthalpy and then obtain the temperature by enthalpy in 3D injection modeling.

4.3.1 The distribution of thermal residual stress

We adopt the cavity as in Fig.4and Shear modulus data as in Table 4 to calculate the thermal residual stress.

Fig. 5 shows the distributions of pressure and thermal residual stress at t=1205 with holding pressure $p_{holding}=10^5$, mold temperature $T_w=313$ and melt temperature $T_m=513$. From Fig. 5, it can be seen that the distributions of residual stress embody the characteristic of the pressure distribution and the values are degressive from the gate to the end of the cavity.

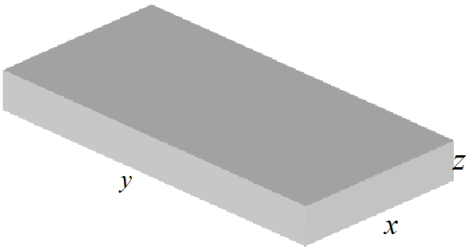

Figure 4: Sketch map and the computational area of the mold

Table 4: Shear modulus data for multi-mode Maxwell model

No. / Variable	1	2	3
θ_i(s)	5.000×10^{-7}	3.099×10^{-3}	2.154×10^{-1}
G_i(Pa)	1.900×10^{8}	0.909×10^{8}	1.460×10^{8}
No. / Variable	4	5	6
θ_i(s)	8.036×10^{0}	3.276×10^{2}	7.626×10^{4}
G_i(Pa)	1.355×10^{8}	1.079×10^{8}	1.538×10^{8}

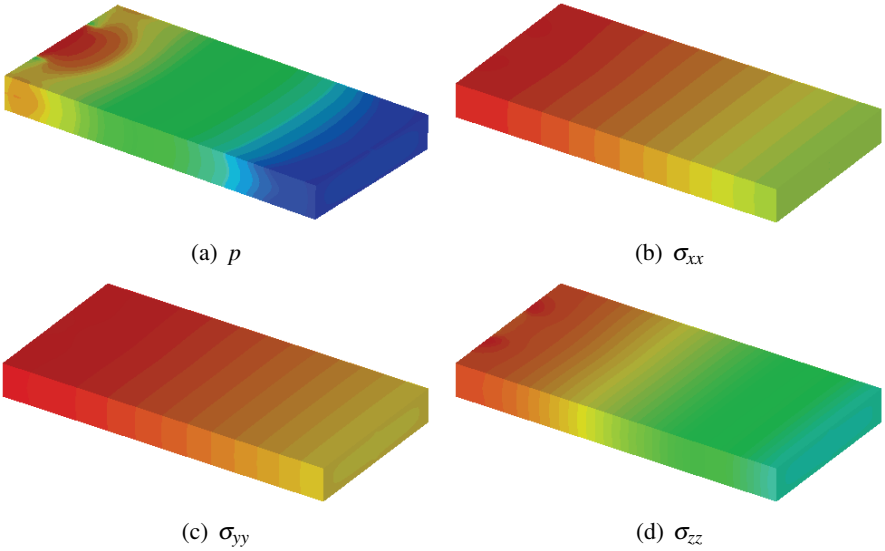

(a) p (b) σ_{xx}

(c) σ_{yy} (d) σ_{zz}

Figure 5: The distributions of pressure and thermal residual stress

Fig. 6 and Fig. 7 show the distributions of temperature and thermal residual stress of x = 2.5 mid-plane and of z=0.5 mid-plane, respectively. It can be seen from Fig. 6 and Fig. 7 the distributions of residual stress imply the characteristic of the temperature distribution. To sum up, the changes of thermal residual stress are influenced by the pressure and temperature in mold cavity, and the phenomenon is consistent with the theoretical analysis in literature [Zheng, Kennedy, Phan-Thien and Fan (1999)].

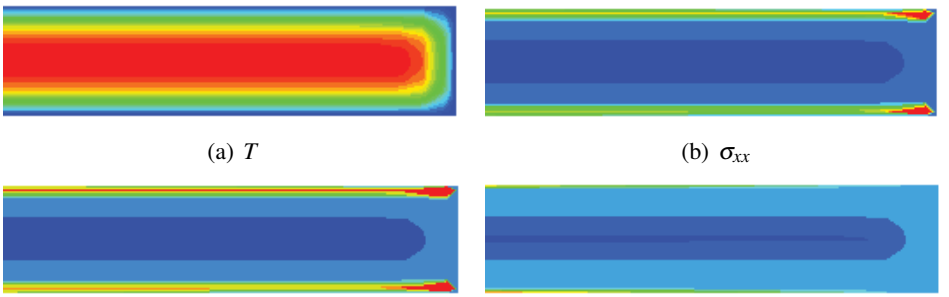

(a) T (b) σ_{xx}

(c) σ_{yy} (d) σ_{zz}

Figure 6: The distributions of temperature and thermal residual stress of x = 2.5 mid-plane

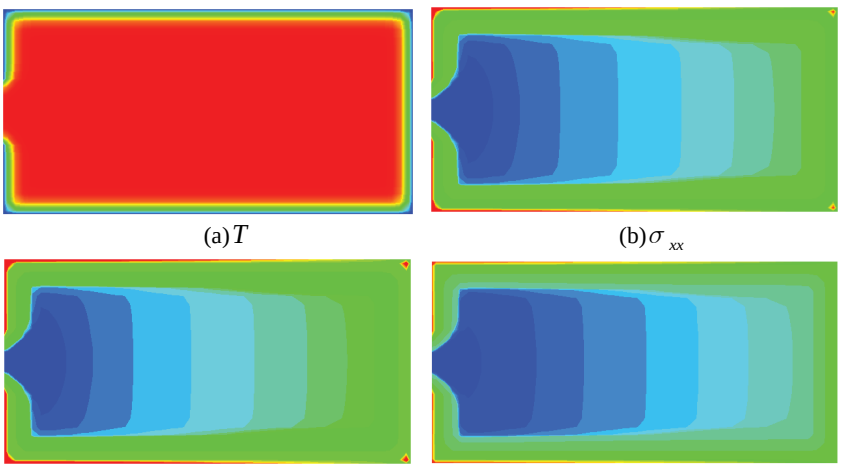

(a) T (b) σ_{xx}

(c) σ_{yy} (d) σ_{zz}

Figure 7: The distributions of temperature and thermal residual stress of z=0.5 mid-plane

The distributions of thermal residual stress along the z-axis are shown in Fig.8. The ordinate value is shrunk to a 1,000 times smaller in Fig. 8 and the same as in the following Figures. In Fig. 8(a), t_1 denotes the time that mold cavity is filled; t_2 denotes the time that pressure of cavity reaches the maximum; $t_3$denotes the time that the melt is almost completely solidified, t_4 denotes the time that the solid is cooled. The evolution of σ_{yy} with time is good agreement with that in the literature [Zoetelief, Douven and Ingen Housz (1996)]. The normal stresses comparisons at time t_4 are shown in Fig. 8(c). It can be clearly seen that the curves shape ofσ_{yy}, σ_{xx} and σ_{zz} are very similar. It's worth noting that the value of σ_{zz} is obviously smaller than those of σ_{yy}andσ_{xx}. This may be both relevant to the less size of thickness and the faster temperature decrease along the direction of thickness.

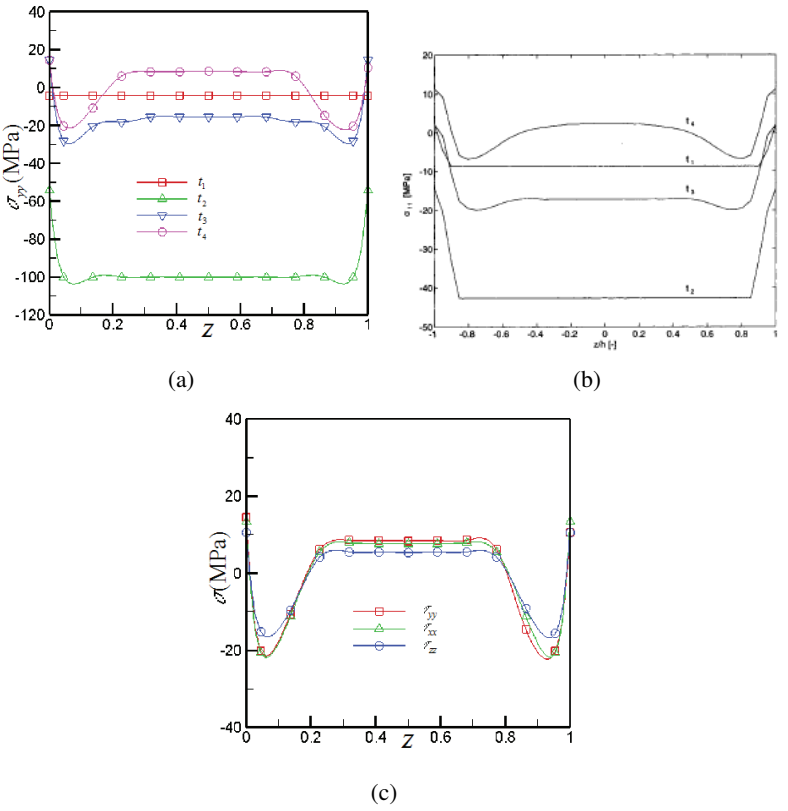

Figure 8: The evolution of $\sigma_{yy}$with time (a):our results,(b) results from [Zoetelief, Douven and Ingen Housz (1996)]and the normal stresses at time t_4(c) along the z-axis.

4.3.2 Influence of processing parameters on thermal residual stress

The processing parameters, especially holding pressure, melt temperature and mold temperature have significant influence on the production of the thermal residual stress in injection molding. The influences of different processing parameters on the thermal residual stress are shown in Fig. 9.

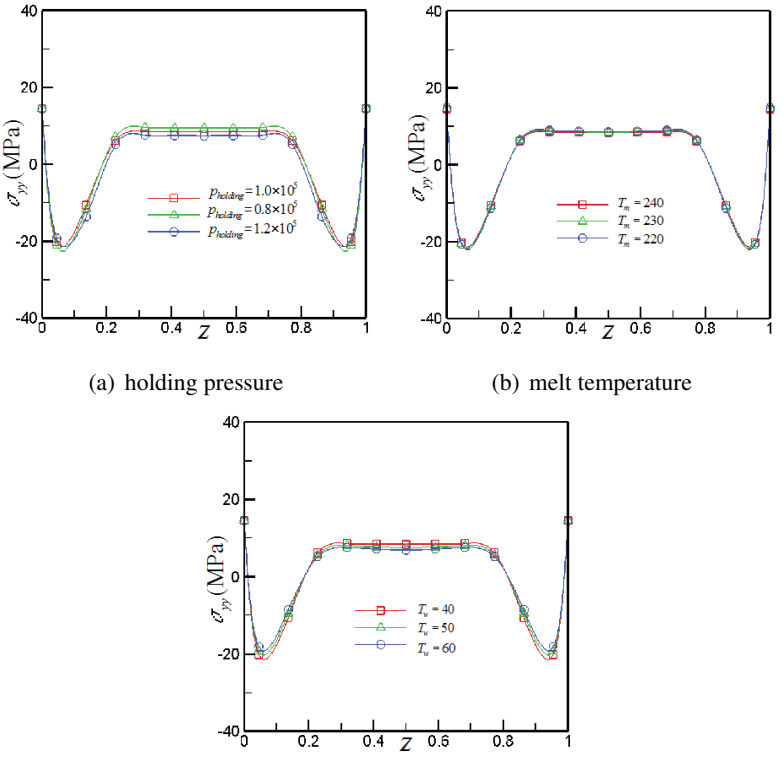

(a) holding pressure

(b) melt temperature

(c) mold temperature

Figure 9: The influences of different processing parameters on σ_{yy}.

Fig. 9(a) shows the residual stress σ_{yy} distribution along z-axis with $T_w = 313$, $T_m = 513$ and different holding pressures. It can be clearly seen that as the values of holding pressure increase, the values of σ_{yy} decrease. Therefore, the holding pressure should be as high as the condition allows for decreasing the residual stress. Fig. 9(b) shows the residual stress σ_{yy} distribution along z-axis with $T_w = 313$, $p_{holding} = 10^5$ and different melt temperatures. It can be seen that the values of σ_{yy} have slightly changes. Fig. 9(c) shows the residual stress σ_{yy} distribution along z-axis with $T_m = 513$, $p_{holding} = 10^5$ and different mold temperatures. It can be

clearly seen that the values of σ_{yy} decrease with the values of mold temperature increase.

5 Warpage simulations

5.1 Warpage Calculation Model

The $\boldsymbol{\sigma}$ in formula (15) denotes the thermal residual stress before the product is released from the mold. However, the temperatures of products continue to decrease until room temperature after demolding. If we mark the difference of temperature as ΔT, the stress from ΔT is $3K\alpha\mathbf{I}\Delta T$ and K is the bulk modulus. Moreover, since the shrinkage of the product is no longer restricted after demolding, the relaxed stress results in the warpage of the product. Therefore, the relation of stress-strain can be written as [Choi and Im (1999)]

$$\boldsymbol{\sigma}^r = \mathbf{D}\boldsymbol{\varepsilon} - 3K\alpha\mathbf{I}\Delta T + \boldsymbol{\sigma} \tag{31}$$

where $\boldsymbol{\sigma}^r = \begin{bmatrix} \sigma_{11}^r & \sigma_{22}^r & \sigma_{33}^r & \sigma_{12}^r & \sigma_{23}^r & \sigma_{31}^r \end{bmatrix}^T$, $\mathbf{I} = [1 \quad 1 \quad 1 \quad 0 \quad 0 \quad 0]^T$, $\mathbf{D}$ is the 3D elastic matrix and the values of components are determined by elastic modulus E and Poisson's ratio ν. The $\mathbf{D}$ matrix and K are given as follow

$$\mathbf{D} = \frac{E}{(1+\nu)(1-2\nu)} \begin{bmatrix} 1-\nu & \nu & \nu & 0 & 0 & 0 \\ \nu & 1-\nu & \nu & 0 & 0 & 0 \\ \nu & \nu & 1-\nu & 0 & 0 & 0 \\ 0 & 0 & 0 & (1-2\nu)/2 & 0 & 0 \\ 0 & 0 & 0 & 0 & (1-2\nu)/2 & 0 \\ 0 & 0 & 0 & 0 & 0 & (1-2\nu)/2 \end{bmatrix},$$

$$K = \frac{E}{3(1-2\nu)}.$$

According to formulas (26) and (29), formula (31) can be rewritten as

$$\left(\mathbf{A}^T\mathbf{D}\mathbf{A}\right)\mathbf{d} = 3K\alpha\mathbf{A}^T\mathbf{I}\Delta T - \mathbf{A}^T\boldsymbol{\sigma}^r - \mathbf{F} \tag{32}$$

Formula (2) is the calculation model of warpage. $\mathbf{F} = \begin{bmatrix} F_{b1} & F_{b2} & F_{b3} \end{bmatrix}^T$ is zero for warpage problem. Moreover, the boundary conditions of warpage are free boundary conditions because the deformation of product is free after demolding.

5.2 The modified FENN Method for warpage

The idea of FENN method is to embed the finite element discrete model in a neural network structure. It derives the neural network using the energy functional resulting from the finite-element formulation based on error minimization. The details will be precisely delineated in subsequent sections.

5.2.1 FEM discretization

If the computational region is Ω and the $\mathbf{F}$ is zero in formula (32), the weak form of (32) can be written as

$$\iiint_{\Omega} \left(\left(\mathbf{A}^T \mathbf{D} \mathbf{A} \right) \ \mathbf{d} \right) dxdydz = \iiint_{\Omega} \left(3K\alpha \mathbf{A}^T \mathbf{I} \Delta T - \mathbf{A}^T \boldsymbol{\sigma} \right) dxdydz \tag{33}$$

The 8-nodes hexahedral element is used for spatial discretization. The primitive unknown variable $\mathbf{d}$ is spatially approximated using standard finite element shape functions $\mathbf{N}$ and expressed in terms of their nodal values $\overline{\mathbf{d}}$ as

$$\mathbf{d} = N_{dj} \overline{\mathbf{d}}_j, \quad j = 1, 2, \ldots, 8 \tag{34}$$

The strain matrix of formulas (25) on an element is

$$\mathbf{B} = \left[\mathbf{B}_1 \ \ \mathbf{B}_2 \ \ldots \ \mathbf{B}_m \right] \tag{35}$$

where $\mathbf{B}_i = \begin{bmatrix} \frac{\partial N_i}{\partial x} & 0 & 0 & \frac{\partial N_i}{\partial y} & 0 & \frac{\partial N_i}{\partial z} \\ 0 & \frac{\partial N_i}{\partial y} & 0 & \frac{\partial N_i}{\partial x} & \frac{\partial N_i}{\partial z} & 0 \\ 0 & 0 & \frac{\partial N_i}{\partial z} & 0 & \frac{\partial N_i}{\partial y} & \frac{\partial N_i}{\partial x} \end{bmatrix}^T$.

The stiffness matrix on an element is

$$\mathbf{K}^e = \iiint_{\Omega^e} \mathbf{B}^T \mathbf{D} \mathbf{B} dxdydz \tag{36}$$

where $\mathbf{K}^e_{ij} = \iiint_{\Omega^e} \mathbf{B}_i^T \mathbf{D} \mathbf{B}_j dxdydz$. The total stiffness matrix is

$$\mathbf{K}_{ij} = \sum_{e=1}^{M} \mathbf{K}^e_{ij} \tag{37}$$

The right term on an element is

$$\mathbf{b}^e_i = \iiint_{\Omega^e} \mathbf{B}_i^T \left(3K\alpha \mathbf{I} \Delta T - \sigma \right) dxdydz \tag{38}$$

The total right term is

$$\mathbf{b}_i = \sum_{e=1}^{M} \mathbf{b}^e_i \tag{39}$$

After the discretization in FEM formulation, Eq. (33) is transformed into the following linear equations

$$\mathbf{K}\mathbf{d} = \mathbf{b} \tag{40}$$

5.2.2 The structure design of FENN

The structure design of FENN is shown in Fig.10. M and N correspond to the numbers of discrete elements and nodes in finite element method.

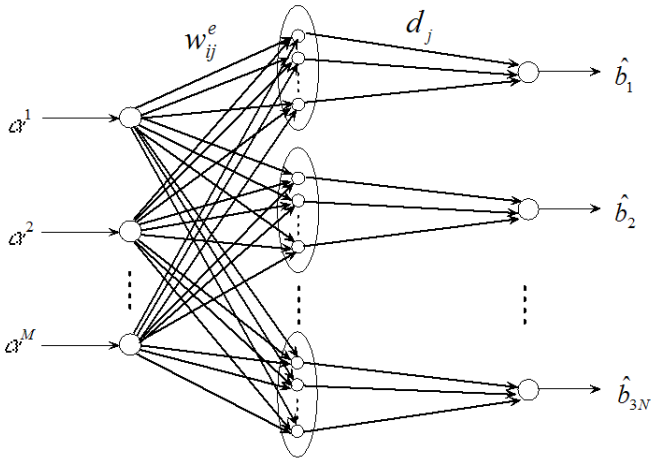

Figure 10: The structure design of FENN

The inputs of input layer are $\alpha^1 = \alpha^2 = \cdots = \alpha^M = 1$. The weighs between the input layer and hidden layer is $w_{ij}^e = \mathbf{K}_{ij}^e$ and w_{ij}^e is constant when the finite element mesh and shape function remain unchanged. The active function of hidden layer is constant 1, and the output of hidden layer is $\mathbf{K}_{ij} = \sum_{e=1}^{M} w_{ij}^e$. The weighs between the hidden layer and output layer is d_j, the ith output of the neural network is $\hat{b}_i = \sum_{j=1}^{L} K_{ij} \times d_j$. Therefore, FENN has M neurons in input layer, 3N×L neurons in hidden layer and 3N neurons in output layer. Where, L is the bandwidth of stiffness matrix. The subjective function of FENN is

$$E(t) = \left\| \hat{\mathbf{b}}(t) - \mathbf{b} \right\| \tag{41}$$

The weight d_j needs to be optimized in FENN. The particle swarm optimization is used to optimize d_j to overcome the shortcomings of traditional gradient descending method, such as falling easily into local optimal solution and slower convergence speed. In particle swarm optimization, the update formulas of velocity, position and inertia weight are [Li, Ouyang, Yang and Jiang (2010)]

$$V_i(t+1) = WV_i(t) + C_1 r_1(t)\left[P_i(t) - X_i(t)\right] + C_2 r_2(t)\left[P_g(t) - X_i(t)\right] \tag{42}$$

$$X_i(t+1) = X_i(t) + V_i(t+1) \tag{43}$$

$$w_{ij} = 1 - rand() \left(\frac{1}{1+e^{-I_{ij}}} \right) \quad I_{ij} = \frac{\left| x_{ij} - p_{ij} \right|}{\left| p_{ij} - p_{gj} \right| + \varepsilon}, \tag{44}$$

where rand ( ) is a random number in the interval of [0, 1]; x_{ij} is the position of the ith particle in the jth dimension; p_{ij} is the own best solution, while p_{gj} is the current global best solution; ε is a positive constant close enough to zero; α is a positive constant in the range (0,1].

5.2.3 The calculation steps of FENN

The detailed numerical steps for solving 3D warpage are summarized as follow:

Step1: Choose the type of the element, determine the numbers of elements M and nodes N;

Step2: Calculate per output of neurons of hidden layer;

Step3: Set the size of population (Pn) and the terminating condition of FENN (ε); Initialize the position and velocity of the particles in admissible parameter spaces randomly;

Step4: Initialize the variable of iteration: t =1;

Step5: Initialize the variable of the particle iteration: i=1;

Step6: Set the weights (d_j) of FENN with the best position of the ith particle;

Calculate the output of FENN and the fitness of ith particle ($E_i(t)$), then $i = i$+1;

Step7: If i <Pn, go to Step6; otherwise, evaluate the fitness of each particle and store best position of each particle and the whole particle swarm, then $t = t$+1;

Step8: Calculate the best fitness of the whole particle swarm: $E_{best}(t) = \left\| \hat{\mathbf{b}}(t) - \mathbf{b} \right\|$; If $E_{best}(t) < \varepsilon$, output the results; otherwise, update the position and velocity of each particle and go to Step5.

5.3 Calculation Results

5.3.1 The validation of FENN

To verify the effectiveness of FENN method, two examples of 3D displacement are calculated in this section. The sizes of calculation areas for example 1 and example 2 are 0.2×0.8×0.3 and 0.5×3.0×2.0, respectively. The 3D finite element meshes are shown in Fig. 11. The numbers in Fig. 11 are the global number of the nodes.

In example 1, the displacements in three directions of nodes 1, 2, 5 and 6 are zero; force load along the negative direction of z-axis is 105 N and is exerted on the nodes 7 and 8; elastic modulus$E = 1.0 \times 10^{10}$Pa, Poisson ratio$\nu = 0.25$.

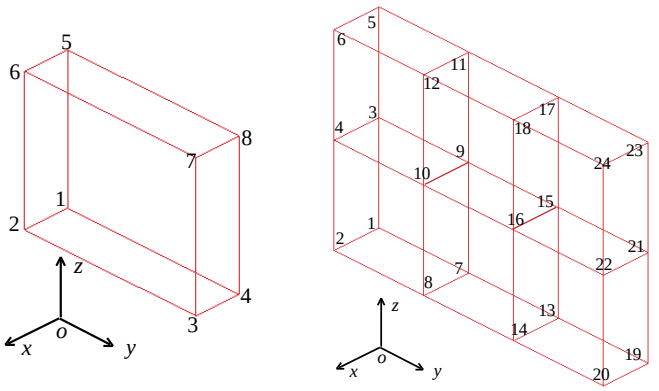

(a) example 1 (b) example 2

Figure 11: The finite element mesh

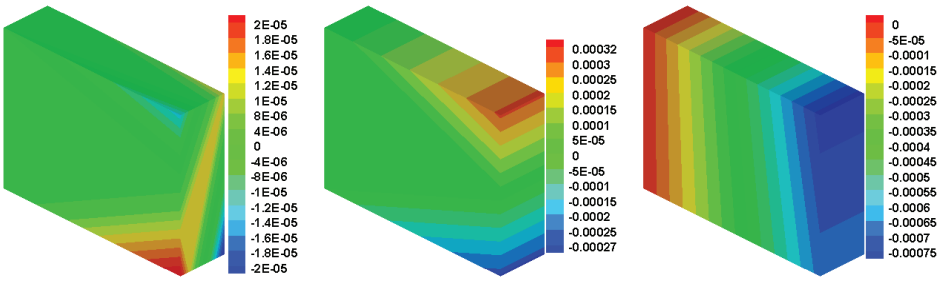

(a) d_1 (b) d_2 (c) d_3

Figure 12: The 3D displacement distributions of example 1

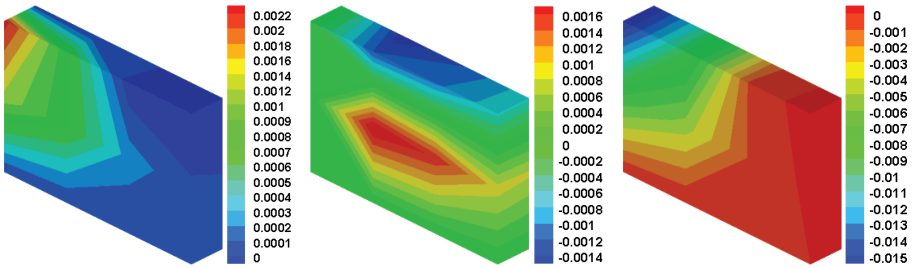

(a) d_1 (b) d_2 (c) d_3

Figure 13: The 3D displacement distributions of example 2

The 3D displacement distributions of example 1 are shown in Fig. 12. The results comparison of non-zero displacement between FENN and FEM are given in Table 5. The values in Table 5 are magnified 1000 times for better displays than real values. From Table 5, it can be seen that the calculation results of FENN and FEM consistent. Moreover, if the values contain up to 4 digits after the decimal point, the results of FENN and FEM are completely same.

Table 5: The results comparison of non-zero displacement between FENN and FEM

FENN			
Node	d_1	d_2	d_3
3	0.022295	−0.276913	−0.672802
4	−0.022293	−0.276908	−0.672797
7	−0.012911	0.310821	−0.777389
8	0.012884	0.310807	−0.777395
FEM			
Node	d_1	d_2	d_3
3	0.0223499	−0.27687	−0.672764
4	−0.0223499	−0.27687	−0.672764
7	−0.012889	0.310772	−0.777425
8	0.012889	0.310772	−0.777425

In example 2, when x=0, d1=0; when y=0, d2=0; when z=0, d1= d2= d3=0; force load along the negative direction of z-axis is 0.125kN and is exerted on the nodes 5, 6, 11 and 12; elastic modulus $E = 100\text{kN}/\text{m}^2$, Poisson ratio $\nu = 0.3$.

The 3D displacement distributions of example 2 are shown in Fig. 13. The displacement of each node is shown in Table 6. The values in Table 6 are magnified 100 times for better displaying than real values. If the calculation results of FENN contain up to 4 digits after the decimal point, the results are the same as the results of literature [Smith and Griffiths (1988)].

5.3.2 The calculation results of warpage

The material parameters of HDPE Sclair 2714 are $E = 9.11 \times 10^8$Pa, $\nu = 0.426$ and $\alpha = 0.00015$ in calculation of the warpage. The warpage describes the deformations of the product about a fixed point. Here, we choose the middle node of those nodes within gate.

Fig. 14 gives the warpage distribution with$p_{holding} = 10^5$, $T_w = 313$ and $T_m = 513$.

Table 6: The displacement of each node

Node	d_1	d_2	d_3
1	0	0	0
2	0	0	0
3	0	0	−0.653387
4	0.155035	0	−0.684212
5	0	0	−1.59494
6	0.229728	0	−1.61189
7	0	0	0
8	0	0	0
9	0	0.163174	−0.42718
10	0.103009	0.181983	−0.443678
11	0	−0.153021	−0.903392
12	0.105607	−0.11962	−0.90115
Node	d_1	d_2	d_3
13	0	0	0
14	0	0	0
15	0	0.143115	−0.096413
16	0.030998	0.155727	−0.0972196
17	0	−0.119298	−0.110708
18	−0.0136702	−0.105009	−0.0966473
19	0	0	0
20	0	0	0
21	0	0.0848723	0.0265386
22	0.00369352	0.0892407	0.0281824
23	0	−0.0639011	0.0576026
24	−0.0173517	−0.0662872	0.0655168

The displacement in x direction is shown in Fig. 14(a). Due to the mid node of the gate locates the origin of x-axis, the displacement of x direction is symmetrical about the y-axis. The displacement in y direction is shown in Fig. 14(b). From Fig. 14(a) and Fig. 14(b), it can be seen that the maximum values of displacement appear in the location away from the gate. Fig. 14(c) gives the warpage distribution of the product. It can be seen that the maximum values appear in two corners of the product, and the corners are away from the gate. The results are good agreement with the facts.

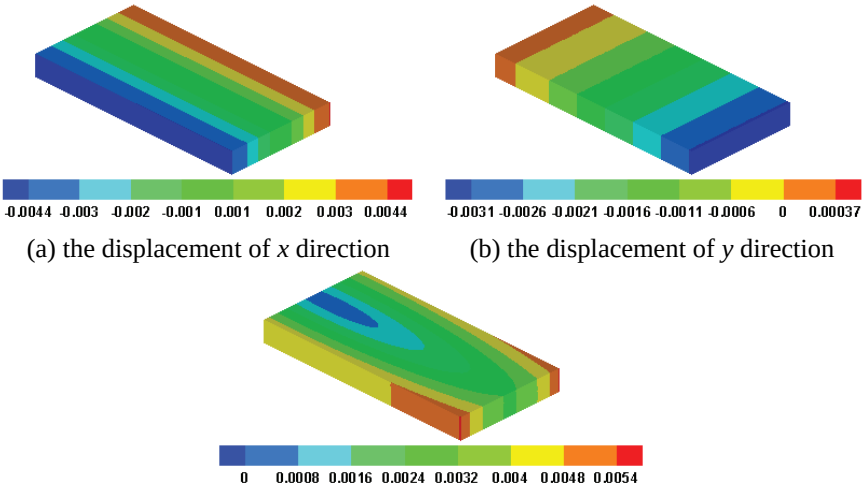

(a) the displacement of x direction (b) the displacement of y direction

(c) warpage of the product

Figure 14: The warpage distribution of the product (unit: mm)

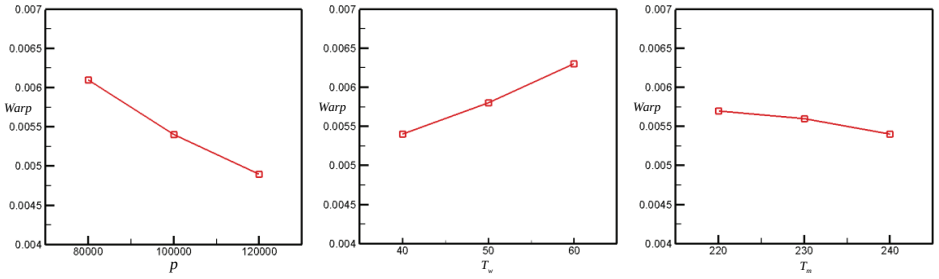

(a) holding pressure (b) mold temperature (c) melt temperature

Figure 15: The influences of different processing parameters on the maximum warpage(unit: mm)

The influences of different processing parameters on the maximum warpage are shown in Fig. 15(a), (b) and (c). Fig. 15(a) shows that the warpage decreases with the increasing of holding pressure. It can be proved that the enough holding pressure can decrease the warpage of the products. From Fig. 15(b), it can be seen that the warpage increases as the mold temperature increases. It may be possible that high mold temperature results in large shrinkage which leads great warpage. The influence of melt temperature on warpage is shown in Fig. 15(c) and the influence of melt temperature is slight.

6 Conclusions

In this paper, the numerical simulation of the thermal residual stress and warpage of injection molding products based on there-dimensional (3D) mathematical models are studied, and the phase-change effect is considered in the calculation of temperature field. The 3D thermal residual stress model is transformed into the incremental displacement model for solving. The 3D warpage mathematical model is solved by a modified FENN. The numerical results show:

(1) There is a steep change for the case with phase-change while there is a smooth change for the case without phase-change in the region of phase-change.

(2) The changes of thermal residual stress are influenced by pressure and temperature in mold cavity, and the phenomenon is consistent with the theoretical analysis in literature [Zheng, Kennedy, Phan-Thien and Fan (1999)]. The evolution of thermal residual stress with time is good agreement with the literature [Zoetelief, Douven and Ingen Housz (1996)].

(3) The values of thermal residual stress decrease with the increasing holding pressure and decrease with the increasing mold temperature. However, thermal residual stress has slightly changes with the changes of melt temperature.

(4) The simulation of warpage proves that the 3D warpage model can describe the warpage of the product and FENN method can solve the 3D warpage model. The maximum values of the product warpage appear in two corners which are away from the gate.

(5) The maximum value of warpage decreases with the increasing of holding pressure and increases with the increasing of mold temperature. The influence of melt temperature on warpage is slight.

Acknowledgement: All the authors would like to acknowledge the National Basic Research Program of China (2012CB025903).

Reference

Baaijens, F. P. T. (1991): Calculation of residual stresses in injection molded products. *Rheologica Acta*, vol.30, no.3, pp. 284–299.

Boitout, F.; Agassant, J. F.; Vincent, H. (1995): Elastic calculation of stresses in injection mold. *International Polymer Processing*, vol. 10, no.3, pp. 237–242.

Bushko, W. C.; Stokes, V. K. (1995): Solidification of thermoviscoelastic melts. Patr I: Formulation of model problem. *Polymer Engineering and Science*, vol. 35, no.4, pp. 351–364.

Chang, R. Y.; Chiou, S. Y. (1995): A Unified K-BKZ Model for Residual Stress

Analysis of Injection Molded Three-Dimensional Thin Shapes. *Polymer Engineering and Science*, vol.35, no.22, pp. 1733–1747.

Chen, X.; Lama, Y. C.; Li, D. Q. (2000): Analysis of thermal residual stress in plastic injection molding. *Journal of Materials Processing Technology*, vol.101, pp. 275–280.

Choi, D. S.; Im, Y. T. (1999): Prediction of shrinkage and warpage in consideration of residual stress in integrated simulation of injection molding. *Composite Structures*, pp.655–665.

Frederico, J. M. F. C.; Patrick, D. A.; Gerrit, W. M. P.; António, M. C.; Han, E. H. M. (2010): Residual stresses in gas-assisted injection molding. *Rheologica Acta*, vol. 149, pp.23–44.

Guo, Z. Y.; Ruan, X. Y.; Peng, Y. H.; Li, D. Q. (2002): Warpage of Injection-Molded Thermoplastics Parts: Numerical Simulation and Experimental Validation. *Journal of Materials Engineering and Performance*, vol.11, no.2, pp.138–144.

Jansen, K. M. B.; Titomanlio, G. (1996) : Effect of pressure history on shrinkage and residuanl stresses-injection with constrained shrinkage. *Polymer Engineering and Science*, vol.36, no.15, pp.2029–2040.

Jansen, K. M. B.; Pantani, R.; Titomanlio, G. (1998): In-mold shrinkage measurements of PS samples with strain geges. *Polymer Engineering and Science*, vol.38, no.2, pp. 254–264.

Kamal, M. R.; Lai-Fook, R. A.; Hernandez-Aguilar, J. R. (2002): Residual Thermal Stresses in Injection Moldings of thermoplastics: A theoretical and experimental study. *Polymer Engineering and Science*, vol.42, no.5, pp. 1098–1114.

Kosec, G.; Sarler, B. (2009): Solution of Phase Change Problems by Collocation with Local Pressure Correction. *CMES: Computer Modeling in Engineering & Sciences*, Vol.47, No.2, pp. 191–216.

Lee, H. K.; Huang, J. C.; Yang, G. E.; Kim, H.G. (2006): Analysis of Residual stress in Thin Wall Injection Molding. *Key Engineering Materials*, vol.306-308, pp. 1331–1336.

Li, D. Q.; Zhou, H. M. (2004): Modelling and simulation of residual stress and warpage in injection moulding. *Proceedings of Institution of Mechanical Engineers: Part C*, vol.218, no.5, pp.521–530.

Li, Q.; Ouyang, J.; Li, X. J.; Wu, G. R.; Yang, B. X. (2011): Numerical Simulation of Gas-assisted Injection Molding Process for A Door Handle. *CMES: Computer Modeling in Engineering & Sciences*, vol.74, no.3, pp.247–267.

Li, X. J.; Ouyang, J.; Li, Q.; Ren, J. L. (2012): Simulations of a Full Three-Dimensional Packing Process and Flow-Induced Stresses in Injection Molding.

Journal of Applied Polymer Science vol.126, no.5, pp. 1532–1545.

Li, X. J.; Ouyang, J.; Yang, B. X.; Jiang, T. (2010): Warpage optimization in injection molding using MPSO-HNN and MPSO algorithm. *Polymer-Plastics Technology and Engineering*, vol.49, no.12, pp. 1247–1256.

Liu, F.; Zhou, H. M.; Li, D. Q. (2009): Numerical Simulations of Residual Stresses and Warpage in Injection Molding. *Journal of Reinforced Plastics and Composites*, vol.28, no.5, pp.571–585.

Ramuhalli, P.; Udpa, L.; Udpa S. S. (2005): Finite-element neural networks for solving differential equations. *IEEE transactions on neural networks*, vol.16, no.6, pp. 1381–1392.

Shen, C. Y.; Li, H. M. (2003): Numerical Simulation for Effects of Injection Mold Cooling on Warpage and Residual Stresses. *Polymer-Plastics Technology and Engineering* vol. 42, no.5, pp. 971–982.

Smith, I. M.; Griffiths, D. V. (1988): Programming the finite element method, University of Manchester, UK, John Wiley & Sons Ltd.

Truex, M. (2011): Numerical Simulation of Liquid-Solid, Solid-Liquid Phase Change Using Finite Element Method in h,p,k Framework with Space-Time Variationally Consistent Integral Forms. University of Kansas, The degree of Master of Science.

Wang, T. H.; Young, W. B. (2005): Study on residual stresses of thin-walled injection molding. *European Polymer Journal*, vol.41, pp.2511–2517.

Wu, H. H.; Zhao, Z. F.; Shen, C. Y. (2008): Creep model on the internal stress calculation of injection molded polymer. *Chinese journal of mechanical engineering*, vol.44, no.12, pp. 221–225.

Yagawa, G.; Okuda, H. (1996): Finite element solutions with feedback network mechanics through direct minimization of energy functionals. *International journal for numerical methods in engineering*, vol.39, pp.213–228.

Yang, B.; Fu, X. R.; Yang, W.; Huang, L.; Yang, M. B.; Feng, J. M. (2008): Numerical Prediction of Phase-Change Heat Conduction of Injection-Molded High Density Polyethylene Thick-Walled Parts Via the Enthalpy Transforming Model With Mushy Zone. *Polymer Engineering and Science*, vol.48, pp.1707–1717.

Yang, B.; Fu, X. R.; Yang, W.; Liang, S. P.; Hu, S.; Yang, M. B. (2009): Simulation of Phase-Change Heat Transfer During Cooling Stage of Gas-Assisted Injection Molding of High-Density Polyethylene via Enthalpy Transformation Approach. *Polymer Engineering and Science*, vol.49, pp. 1234–1242.

Young, W. B. (2004): Residual stress induced by solidification of thermoviscoelastic melts in the postfilling stage. *Journal of Materials Processing Technology*,

vol.145, pp.317–324.

Zheng, R.; Kennedy, P.; Phan-Thien, N.; Fan, X. J. (1999): Thermoviscoelastic Simulation of Thermally and Pressure-induced Stresses in Injection Moulding for the Prediction of Shrinkage and Warpage for Fibre-Reinforced Thermoplastics. *Journal of Non-Newtonian Fluid Mechanics*, vol. 84, no.2-3, pp. 159–190.

Zhou, H.; Xi, G.; Liu, F. (2008): Residual stress simulation of injection molding. *Journal of Materials Engineering and Performance*, vol.17, pp.422–427.

Zhou, H. M.; Wang, Z. Y.; Li, J. H.; Li, D. Q. (2011): A Surface Model-Based Simulation for Warpage of Injection-Molded Parts. *Polymer Engineering and Science*, vol.51, pp.785–794.

Zoetelief, W. F.; Douven, L. F. A.; Ingen Housz, A. J. (1996): Residual thermal stresses in injection molded products. *Polymer Engineering and Science*, vol.36, no.14, pp. 1886–1896.